


Local strain-dependent electronic structure and perpendicular magnetic anisotropy of a MnGaN 2D magnetic monolayer

Yingqiao Ma ^{1,*}, Diego Hunt ^{2,3,*}, Kengyuan Meng,⁴ Tyler Erickson ¹, Fengyuan Yang ⁴,
María Andrea Barral ^{2,3}, Valeria Ferrari ^{2,3} and Arthur R. Smith ^{1,†}

¹*Nanoscale and Quantum Phenomena Institute, Department of Physics and Astronomy, Ohio University, Athens, Ohio 45701, USA*

²*Departamento de Física de la Materia Condensada, G1yA, CAC, Comisión Nacional de Energía Atómica (CNEA), Avenida General Paz 1499 (1650) San Martín, Buenos Aires, Argentina*

³*Instituto de Nanociencia y Nanotecnología INN (CNEA-CONICET), Buenos Aires, Argentina*

⁴*Department of Physics, The Ohio State University, Columbus, Ohio 43210, USA*



(Received 4 January 2020; revised manuscript received 30 March 2020; accepted 4 May 2020; published 22 June 2020)

Local strain-dependent spin-polarized electronic structure of a two-dimensional (2D) magnetic layer is an exciting property for practical applications. For example, it holds the promise for advanced ultrathin spintronic nanodevices with customized electronic and magnetic properties by local strain engineering. Here, we demonstrate that the spin-polarized electronic structure of a 2D manganese gallium nitride (MnGaN-2D) magnetic monolayer is sensitive to intrinsic local lattice strain, as proven by first-principles calculations and indicated by scanning tunneling spectroscopy measurements. Atomic resolution images reveal a highly non-Gaussian lattice spacing/strain distribution, while the spectroscopy reveals variations in the electronic density of states. Simulations of the MnGaN-2D monolayer based on first-principles calculations, including both isotropic and anisotropic strains, confirm a highly strain-dependent manganese partial density of states. Spin-orbit coupling is included which indicates either *out-of-plane* perpendicular magnetic anisotropy (PMA) or *in-plane* magnetic anisotropy, dependent on the type of strain whether compressive or tensile, suggesting that MnGaN-2D is magnetoelastic. The MnGaN-2D PMA is further supported by superconducting quantum interference device magnetometry measurements which reveal a high spin polarization of $\sim 79\%$ at room temperature.

DOI: [10.1103/PhysRevMaterials.4.064006](https://doi.org/10.1103/PhysRevMaterials.4.064006)

I. INTRODUCTION

The electronic, magnetic, and optical properties of materials are mainly determined by their fundamental lattice structures, and strain engineering is a viable approach to control such properties for better performance in industrial applications. This is particularly true for two-dimensional (2D) crystals [1–3] since usually 2D materials are more flexible with higher elasticity and Young's modulus than most three-dimensional (3D) crystals [4,5]. And due to the 2D nature with reduced neighboring coordinates, their electronic structures are more sensitive to local lattice strain. From the fundamental science point of view, strain-dependent electronic structure of 2D materials could open a new pathway to explore exotic physical phenomena in the quantum regime at the nanoscale, such as the pseudocolossal magnetic field and zero-field quantum Hall effect in graphene [6,7].

Spintronics has been a rapidly developing field around the world in the past decades with broad interests for both basic research and practical applications [8–13]. Two-dimensional materials combining conventional semiconductors and ferromagnetism with high Curie temperature T_C above room

temperature is a highly promising approach for next-generation practical spintronic devices such as nonvolatile magnetic memories with increased densities and for quantum logic chips [14,15]. Strong spin polarization and perpendicular magnetic anisotropy (PMA) are crucial for spintronic materials since the performance of spintronic devices is highly dependent on the spin polarization and since PMA is critical for the design of magnetoresistive random access memory (MRAM) and spin-transfer torque MRAM. This is because materials with PMA usually have larger anisotropy energies, more uniform and stable thermal performance, and require smaller writing currents as compared to most *in-plane* magnetic anisotropy materials.

Two-dimensional diluted magnetic semiconductors were predicted by Cheng *et al.*, including Mn, Fe, Co, and Zn doping of MoS₂ [16]. In general, the observation of monolayer ferromagnetism in any system has been a long-standing objective in reduced-dimensional systems [17,18], especially at room-temperature (RT). In late 2017 we demonstrated, using spin-polarized scanning tunneling microscopy/spectroscopy (SP-STM/STS) combined with first-principles theoretical calculations, RT ferromagnetism with high spin polarization in a monolayer of MnGaN atop a wurtzite GaN substrate [19]. Ferromagnetism at RT has subsequently been reported for several atomically thin dichalcogenide material systems, including MnSe_x and in VSe₂ [20,21]. In this paper, the MnGaN-2D

*These authors contributed equally to this work.

†ohiousmith@gmail.com

monolayer magnetic properties are further quantitatively studied by superconducting quantum interference device (SQUID) magnetometry, which reveals PMA and a strong spin polarization of 79%. Furthermore, by combining STM/STS results and DFT calculations, we demonstrate that the MnGaN-2D monolayer has local, strain-dependent electronic properties and a magnetic anisotropy which also depends in principle on the local lattice strain.

II. METHODS

A. Experimental methods

As demonstrated previously, the MnGaN-2D monolayer can be achieved by depositing ~ 0.4 ML Mn onto the annealed GaN(000 $\bar{1}$) 1×1 surface at ~ 200 °C [19,22]. Once prepared, the sample is then transferred *in situ* for ultrahigh vacuum STM, and also *ex situ* for SQUID magnetometry. No capping layers were added onto the MnGaN-2D surface to avoid inducing any possible extrinsic magnetism and to prevent destroying the MnGaN-2D magnetic properties. Strong oxidation in air is not expected to happen for Mn or Ga in the MnGaN-2D surface at room temperature, and manganese oxide and gallium oxide are not ferromagnetic. It is also necessary to see if the MnGaN-2D magnetic properties could survive after exposure to air, which is critical for practical spintronic applications. For the purpose of uniform heating during growth, each sapphire substrate is coated with a Ti thin film with a uniform thickness around 150 nm on the backside.

Quantum Design MPMS XL is used for SQUID magnetometry measurements with the reciprocating sample option (RSO). The $M(H)$ loops are measured with the method of max slope position and linear regression fitting parameters to eliminate centering errors at zero moment. To subtract the SQUID background contribution, the following equation is used to fit the SQUID raw data beyond the MnGaN-2D saturation field to protect the ferromagnetic range:

$$M(H) = A_{\text{dia}}H + A_{\text{para}}B_{5/2}(5g^*\mu_B H/2k_B T) + \text{sign}(H)M_{(\text{sat})}$$

with four fitting parameters: A_{dia} , A_{para} , g^* , and $M_{(\text{sat})}$. The first term in the equation is the diamagnetic background, the second is the paramagnetic background described by a Brillouin function with $J = \frac{5}{2}$ for Mn, and g^* is the effective g factor, and the third is the saturated ferromagnetic contribution [20]. When the fitting is finished, the ferromagnetic hysteresis loop can be produced by subtracting the diamagnetic and paramagnetic contributions away from the SQUID raw data.

For STS measurements, first the tip is stabilized at V_{stab} which is -0.900 V, and then the feedback loop is turned off, and the dI/dV signal is measured through a lock-in amplifier as a function of the applied bias voltage V . To acquire a better approximation of the sample local density of states (LDOS), the dI/dV spectroscopy values are normalized by dividing by I/V which is the total conductance averaged over voltage [23,24].

B. Theoretical methods

All calculations in this paper employ density functional theory (DFT) within the local density approximation, using the exchange-correlation potential of Ceperley-Adler [25]

as parametrized by Perdew and Zunger [26]. Separable, norm-conserving pseudopotentials of the Troullier-Martins type [27] in the Kleinman-Bylander form [28] are used to describe the effect of the core electrons. Nonlinear core corrections [29] and relativistic effects are included in the pseudopotential generation.

For collinear calculations, we use the DFT method as implemented in the SIESTA code [30] where the valence wave functions are expanded in a basis set of localized atomic orbitals for every atom. Details of the pseudopotentials and numerical atomic orbitals are given in Refs. [31,32]. Non-collinear calculations including spin-orbit coupling [33] are then performed with the implementation of the QUANTUM ESPRESSO code [34] which uses plane-wave basis functions. For Ga atoms, the $3d$ electrons are included in the core. For all calculations, the pseudopotential core radii for Ga are 2, 2.5, and 1.9 Bohr for the s , p , and d orbitals, respectively, while for N the radii are 1.3 Bohr for the s orbitals and 1.45 Bohr for the p orbitals. For the Mn atoms, the $3s^2$ and $3p^6$ states are explicitly included in the calculations where the core radii are 1.7, 1.9, and 1.6 Bohr for the s , p , and d states.

Simulations are carried out for MnGaN-2D slab supercells with 19 layers and a vacuum region of 15 Å. A detailed explanation of the $\sqrt{3} \times \sqrt{3}$ unit cell is given in Ref. [22]. The sampling of the Brillouin zone has a Monkhorst-Pack grid that was checked for convergence with respect to the number of k points. An energy cutoff of 400 Ry and a $6 \times 6 \times 1$ k -point mesh is used. To improve the numerical convergence, a first-order Methfessel-Paxton spreading was implemented. The 10 topmost layers of the slab are relaxed, while the other atoms of the structure are kept fixed to the positions corresponding to the bulk GaN crystal. An energy threshold of 10^{-6} a.u. is used as the convergence criterium for geometry optimization and a threshold of 10^{-3} a.u. for the forces.

III. RESULTS AND DISCUSSION

A. Surface structure

The MnGaN-2D unique well-ordered hexagonal-like bonding structure with uniaxial symmetry is shown in Fig. 1(a) which is based on first-principles theoretical calculations [22]. Both the top and side views are presented, and one can see from the side view that both the Mn-N and Ga-N bonds are tilted away from [000 $\bar{1}$], and the angles vary from point to point within the unit cell. Mn atom spin vectors depicted in the model are based on both first-principles calculations and on SP-STM measurements reported by Ma *et al.* [19] and as shown in the following, are also based on SQUID magnetometry measurements.

Figure 1(b) exhibits the as-grown MnGaN-2D signature reflection high-energy electron diffraction (RHEED) patterns, which indicate the formation of a well-ordered MnGaN-2D monolayer. The $3 \times$ pattern along the [10 $\bar{1}$ 0] direction spontaneously appears upon deposition of Mn onto the well-ordered 1×1 structure. The streaky appearance of the RHEED pattern indicates an atomically smooth surface.

The surface structure of MnGaN-2D is shown in Fig. 1(c). This image shows the hexagonal-like structure of the surface and also the local surface structure variations which result

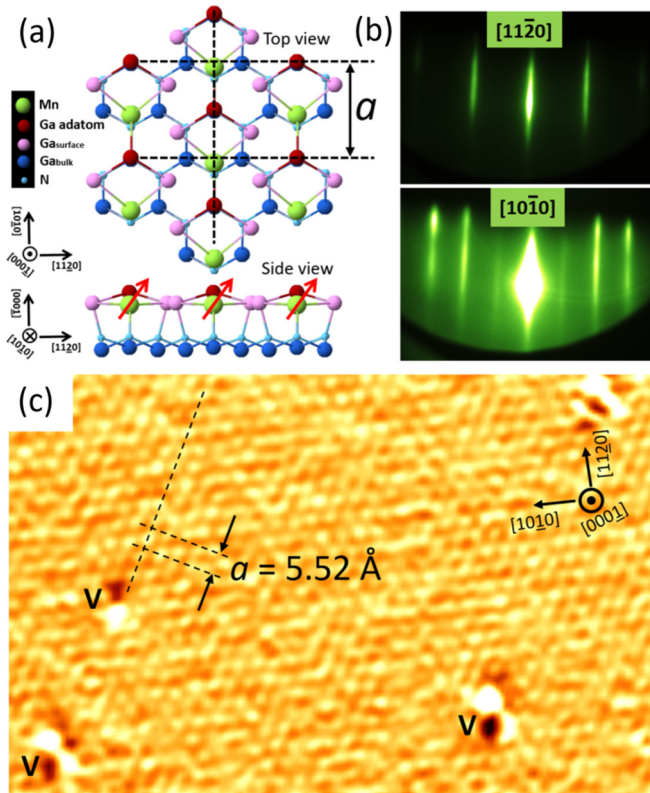


FIG. 1. Structural properties of the MnGaN-2D sample. (a) Top and side views of the MnGaN-2D lattice structure. Signature RHEED patterns of the as-grown MnGaN-2D sample are shown in (b) along the $[10\bar{1}0]$ direction (bottom panel) and along the $[11\bar{2}0]$ direction (top panel). (c) Derivative, constant-current STM image ($V_S = -1.60$ V, $I_T = 100$ pA) of MnGaN-2D showing the hexagonal-like structure with surface variations and a few vacancy defects labeled as “V.”

from the tilted Mn-N and Ga-N bonds shown in the theoretical model in Fig. 1(a) (side view). The surface electron density comes mainly from a combination of Mn and Ga surface states, while the underlying N states are hardly accessible in the STM measurements. Despite the complexity of the surface structure, the hexagonal ordering of the surface layer is seen clearly, and there are very few surface vacancy defects except at those locations labeled in the figure as “V.”

B. Magnetometry measurements

The MnGaN-2D raw SQUID curves measured at 10 and 300 K are presented in Figs. 2(a) and 2(b), which both show clear ferromagnetic contributions with background signals [20]. The corresponding processed MnGaN-2D magnetic hysteresis loops after background subtraction are shown in Figs. 2(c) and 2(d) (see Methods for details) revealing evident ferromagnetism at both 10 and 300 K, which agrees with our previous SP-STM/STS results and spin-polarized DFT calculations, and further proves the room-temperature ferromagnetic nature of the MnGaN-2D monolayer [19]. Furthermore, by looking at Figs. 2(c) and 2(d), the previously suspected PMA is now clearly observed [19], as the

out-of-plane (OOP) hysteresis loops are faster to be saturated than the *in-plane* (IP) loops, and with higher residue moments.

Consistent ferromagnetic response is achieved in several other MnGaN-2D samples as shown in Table I, where it can be seen that although the magnetic moment per Mn atom is only slightly reduced by $\sim 1.5\%$ going from 10 to 300 K, the remanent value is reduced by $\sim 30\%$ going from 10 to 300 K, for both IP and OOP. Based on the values of IP and OOP magnetic remanence shown in Table I, the magnetic anisotropy angle of about 54° away from the surface IP direction can be easily calculated as $\tan^{-1}(\frac{M_{OOP}}{M_{IP}})$, in which M_{OOP} and M_{IP} are the magnetic remanence values of the OOP and IP hysteresis loops.

To further rule out any possible extrinsic origins of the observed ferromagnetism in SQUID measurements, control experiments are performed. The control sample is a bare annealed GaN(000 $\bar{1}$) 1×1 base layer, which is grown, transferred, and measured in the exactly same way as MnGaN-2D samples, only without submonolayer Mn. Figure 3(a) plots the raw SQUID curves of the GaN control sample at 10 K and the MnGaN-2D sample at both 10 and 300 K with the *out-of-plane* field, which reveals a straight line of diamagnetic response without any obvious ferromagnetism for the GaN control sample, as compared to the MnGaN-2D sample. Another GaN(000 $\bar{1}$) control sample shows consistent behavior. As a result, the intrinsic nature of the MnGaN-2D ferromagnetism is demonstrated.

The corresponding processed SQUID loops of Fig. 3(a) are plotted in Fig. 3(b). After subtracting the background signal, the GaN control sample reveals partial hysteretic response with a saturation moment of $\sim 1.65 \times 10^{-5}$ emu/cm 2 . However, it is weaker and not as well defined as compared to the MnGaN-2D hysteresis loop with a saturation moment of $\sim 3.27 \times 10^{-5}$ emu/cm 2 . The small ferromagnetic signal of the control sample could come from the magnetic impurities in the sapphire substrate, GaN base layer, or the Ti backcoating. Therefore, by subtracting the GaN control sample saturation moment away from the MnGaN-2D sample saturation moment, the intrinsic MnGaN-2D monolayer contribution of $\sim 1.62 \times 10^{-5}$ emu/cm 2 can be obtained. And dividing by the amount of Mn deposited (0.4 ML) corresponding to 4.43×10^{14} Mn/cm 2 , a magnetic moment of $\sim 3.94 \mu_B$ per Mn atom is calculated for the MnGaN-2D magnetic monolayer, which is consistent with a previous calculated value of $3.80 \mu_B$ per Mn [19]. This value is large as compared to $\sim 2.12 \mu_B$ per Fe in bulk iron. Since the spin polarization is roughly proportional to the magnetic moment per atom, based on the theoretical limit of $5 \mu_B$ per Mn, a large spin polarization of $\sim 79\%$ can be calculated (as compared to $\sim 40\%$ for bulk Fe), thus quantitatively proving the strong spin polarization in the MnGaN-2D magnetic monolayer.

C. STM dI/dV spectroscopy

Next, the MnGaN-2D spin-polarized electronic structure showing clear variations in filled states is observed in two sets of normalized differential tunneling conductance curves (dI/dV)/ (I/V) taken on the MnGaN-2D surface, as shown in Figs. 4(a) and 4(b). Corresponding I/V and dI/dV curve

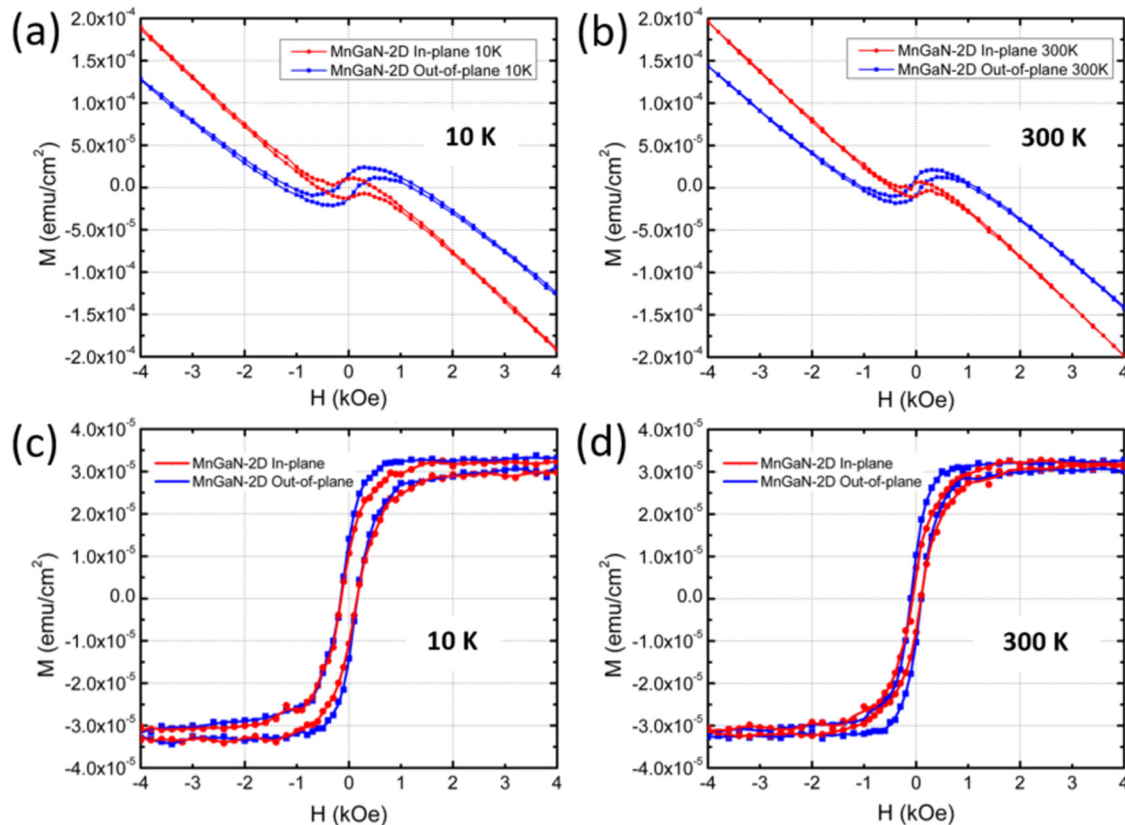


FIG. 2. SQUID measurements of the MnGaN-2D sample. Unprocessed SQUID data are shown in (a) at 10 K and (b) at 300 K. The red and blue hysteresis curves are taken, respectively, under applied *in-plane* and *out-of-plane* magnetic fields. Their corresponding processed magnetic hysteresis loops are plotted in (c) and (d) after background subtraction.

data for Figs. 4(a) and 4(b) are shown in the Supplemental Material, Fig. S1 [35]. The overall shape of the normalized conductance curves is consistent with calculated spin-polarized MnGaN-2D density of states, revealing a strong filled states Mn peak (FSMP) and a broader empty states Mn peak (ESMP). These Mn states are both spin-polarized and spin split [19]. We see from these two sets of spectra that the energy position of the FSMP (E_{FSMP}) varies from spectrum to spectrum. The black (lower) curve barely reveals the FSMP as it is right near the edge of the spectrum window in both Figs. 4(a) and 4(b), and close to -1.69 and -1.70 eV, respectively. The other three curves [red, blue, green in Fig. 4(a) and red, blue, magenta in Fig. 4(b)] correspond to subsequent spectra acquired. These subsequent spectra reveal that E_{FSMP} varies in the range from -1.39 to -1.22 eV [Fig. 4(a)] and from -1.55 to -1.38 eV [Fig. 4(b)]. Not only are the

energy ranges different, but the Mn-states peak shapes are also different, with the Mn-states peaks in Fig. 4(b) being less sharp compared to those in Fig. 4(a).

It can also be noticed that the ESMP near $+1.40$ eV which is visible in Fig. 4(a) does not really move from spectrum to spectrum. For the Fig. 4(b) data, at positive bias no clear peak is revealed, but possibly we see the left shoulder of a broader peak which may or may not correspond to the ESMP seen in Fig. 4(a). In any case, we do not establish any variations of the ESMP energy (E_{ESMP}) in either the Fig. 4(a) or Fig. 4(b) data, while E_{FSMP} clearly shifts.

How to explain the shifts seen for E_{FSMP} is by considering various possibilities. One possibility which may be considered is a charging effect. Supposing that the surface was semi-conducting and that there were some defects or electronic impurities within the surface, there is the possibility that

TABLE I. MnGaN-2D magnetic properties for two samples based on SQUID measurements. Sample A corresponds to the data shown in Fig. 1.

	IP saturation field (kOe)	OOP saturation field (kOe)	IP magnetic remanence (emu/cm ²)	OOP magnetic remanence (emu/cm ²)	Magnetic moment per Mn (a)	Magnetic anisotropy angle (deg)
Sample A at 10 K	1.34	0.69	1.04	1.45	3.94	54.4
Sample A at 300 K	1.77	0.72	0.74	1.01	3.88	53.8
Sample B at 10 K	1.25	0.87	1.01	1.37	3.76	53.6
Sample B at 300 K	1.58	0.96	0.71	0.94	3.71	52.9

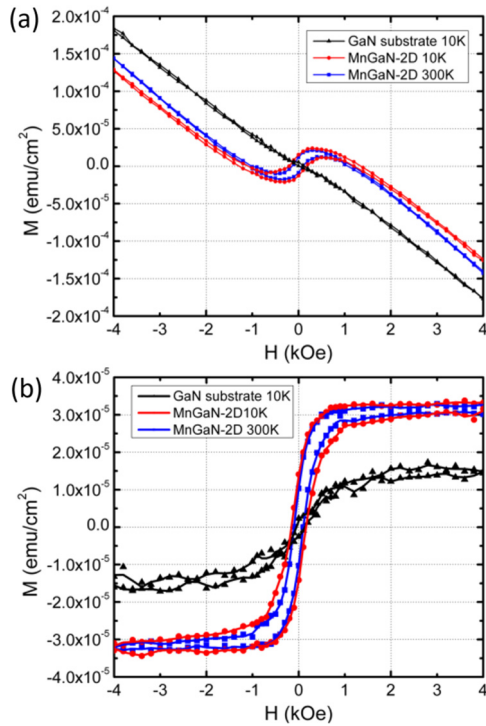


FIG. 3. SQUID measurements of the GaN control sample as compared to the MnGaN-2D sample. (a) The raw SQUID data taken under an *out-of-plane* magnetic field for a bare GaN(000 $\bar{1}$) control sample at 10 K (black curve) and for a MnGaN-2D sample at 10 K (blue curve) and at 300 K (red curve). (b) Processed, background-subtracted magnetic hysteresis curves corresponding to the curves in (a).

injecting electrons into the surface (positive sample bias) could lead to some negatively charged defect sites. If so, this could lead to energy shifts of the electronic structure while in the vicinity of those sites, simply because it would change the local electrochemical potential, via a repulsive Coulombic interaction between the tunneling electrons and the negative surface charges. This could lead to an energy shift of up to a few tenths of eV. And one should then expect to find local variations of the density of states in the form of long-range topographic distortions (LTD's) sometimes seen in STM images of semiconducting surfaces. Indeed, we have previously reported STM images of MnGaN-2D showing such LTD's at positive sample biases [19].

One difficulty with the charging hypothesis is the timescale of the peak shifting. If the surface contains just one or a few charged defects, with a 1 nA tunnel current (10^{10} electrons per second), the time to charge would be much faster than the time between spectra. The other problem is that although we did observe LTD's at positive sample biases, the shifts of E_{FSMP} occur for negative sample biases. So then, while a charging effect could also potentially take place at negative sample biases, in the following sections we discuss a different possibility based on a strain effect. First, we demonstrate with certainty that there exist large local strain variations within the surface based on direct, atomic resolution STM images of the surface. Second, we carry out first-principles calculations in

order to explore the effect of both global and local strains on the surface local density of states.

D. Direct measurement of local surface strain by STM

Figure 5(a) is the STM topography corresponding to the area where the dI/dV spectra measurements are taken in Fig. 4(a). The cross in Fig. 5(a) marks the starting tip position while taking the series of spectra. These measurements were taken at room temperature. A careful analysis of the drift rate finds $\sim 8.7 \pm 0.6 \times 10^{-4}$ nm/s. During the ~ 15 minutes for this set of dI/dV spectra, the tip would have moved ~ 0.8 nm. Although this is very small, since one lattice spacing corresponds to only 0.55 nm, the tip would have moved across more than one unit cell during the spectroscopy measurements.

An atomic resolution STM image of a typical MnGaN-2D area is shown in Fig. 5(b). One sees significant variations in the local lattice structure, but there is a definite long-range order, as shown by the good match between the perfectly periodic blue dots and the atomic protrusions in the image seen in Fig. 5(b). Occasional lattice defects are seen in a few places on the surface which are circled. To quantitatively analyze the local lattice spacing, dots are overlaid at the precise centers of the atomic protrusions and connected by lines as seen in Fig. 5(c). The resulting network is clearly hexagonal-like with hardly any atoms missing, in good agreement with the theoretical model, but the local variations are easily seen in the image by the red and purple half-unit-cell triangles which have indeed very different sizes.

These lattice-spacing variations directly correspond to local lattice strains. This strain is quantitatively determined by carefully measuring the spacings between blue dots along all three high-symmetry axes of Fig. 5(c) for the MnGaN-2D structure and plotting that as a histogram distribution shown in Fig. 5(d). Based on the model shown in Fig. 1(a), Mn atoms are located along a line in-between a pair of Ga adatoms (protrusions in the STM image); therefore, Mn atoms are under varying amounts of strain, some compressive and some tensile, existing within the MnGaN-2D surface. The lattice-spacing distribution can be turned into a strain distribution using the un-strained nominal a -spacing value $= 5.52$ Å of the MnGaN-2D structure. It is found that the strain distribution varies widely, from $\sim -18\%$ to $+18\%$, corresponding to a -spacing values ranging from 4.5 to 6.5 Å. Over this range, the strain distribution has a characteristic asymmetrical, non-Gaussian shape which is reproduced even after shifting the histogram bin intervals, as seen in Fig. 5(d).

To get a more general view of the longer-range ordering of the surface structure, we carry out a full two-point (pair) correlation analysis, using a pair correlation function application [36]. A graph of the results is plotted in Fig. 5(e) which shows the relative probability of a pair occurring at a specific pair distance. The same pair correlation analysis is carried out for a perfect hexagonal structure having the same average (mean) lattice spacing as for the MnGaN-2D lattice. The results for the MnGaN-2D lattice show a series of peak groupings with mean locations matching those of the sharp peaks of the ideal hexagonal lattice which themselves correspond to 1st, 2nd, 3rd, 4th, 5th,... out to 11th nearest neighbors. Note that the lattice spacing/strain distribution from Fig. 5(d) is reproduced

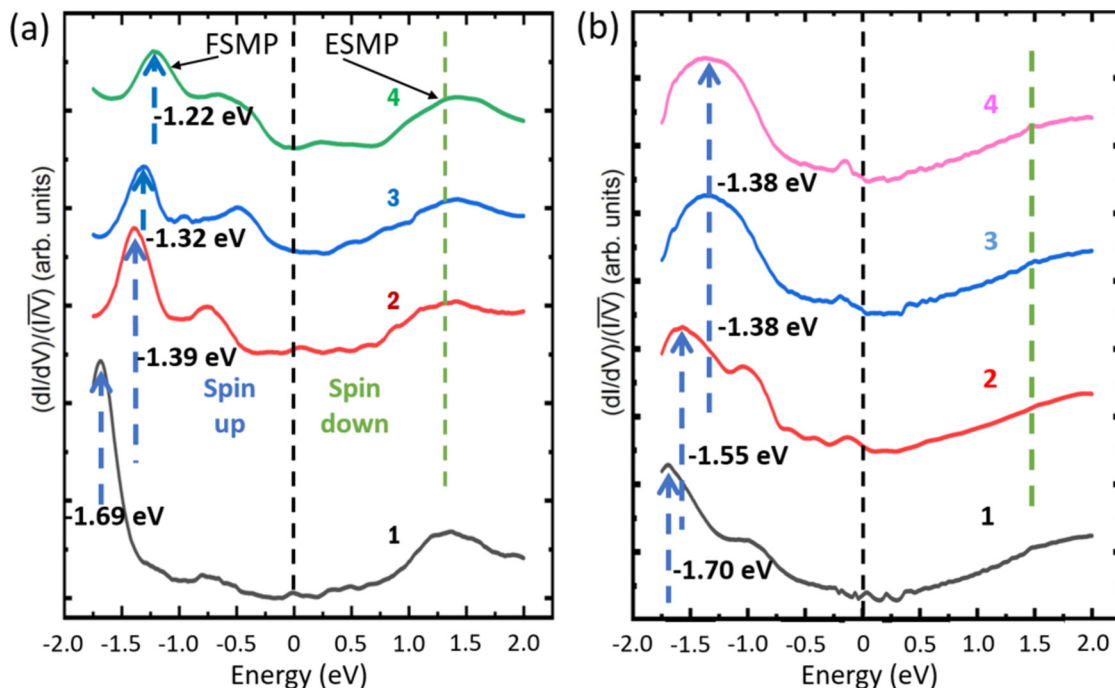


FIG. 4. (a) A series of averaged and normalized tunneling spectra $(dI/dV)/(\overline{I\overline{V}})$ taken at a random location on the MnGaN-2D surface with $V_{\text{stab}} = -0.9$ V, revealing two robust Mn-related peaks, one at the filled-states side indicated by the dashed blue arrows, and the other at the empty-states side indicated by the dashed green line. The filled-states Mn peak (FSMP) shows a shifting energy position, while the empty-states Mn peak (ESMP) stays at one place. (b) Similar $(dI/dV)/(\overline{I\overline{V}})$ spectra taken on a different surface location showing shifts from spectrum to spectrum in the energy position of the FSMP. Numbers 1, 2, 3, and 4 indicate the measurement sequence.

as the first-nearest-neighbor peak grouping in Fig. 5(e). The width of the first-nearest-neighbor peak grouping matches the spread of strain values (-18% to $+18\%$) determined from Fig. 5(d). We also notice that the areas under the peak groups match the areas under the ideal hexagonal neighbor peaks as determined by the correlation function value (CFV) numbers for every neighbor peak. Even the total CFV sums for the entire pair correlation graph for the MnGaN-2D and ideal hexagonal cases agree to within 3.5%. These results prove that the MnGaN-2D structure maintains long-range order as seen clearly in Figs. 5(b) and 5(e), but shows local (short-range) disorder as seen clearly in Figs. 5(c) and 5(d).

E. Theoretical modeling

Since the tip is positioned at slightly different locations on the MnGaN-2D surface, the dI/dV spectra may be modified by the intrinsic local lattice strain variations. To examine this theoretically, we investigate the influence of lattice strain on the Mn partial density of states (PDOS) by performing first-principles DFT calculations for two different strain models: a lateral isotropic strain model (1) and a local anisotropic strain model (2).

1. Lateral isotropic strain model

For the case of lateral isotropic strain, we perform calculations for the MnGaN-2D structure either increasing or decreasing the *in-plane* lattice constant a , to create tensile or compressive strain, respectively. We take the reference of the unstrained case with $a = 5.52$ Å. The Mn PDOS plots are shown in Fig. 6(a) for each of these cases. Interestingly,

it is found that increasing the *in-plane* lattice constant a by 9.1% (tensile strain) decreases the Mn-N bond length ($d_{\text{Mn-N}}$) by 12.8%, whereas decreasing a by 6.0% (compressive strain) increases $d_{\text{Mn-N}}$ by 12.8%. The fact that lateral isotropic strain exerts an opposite effect on the *out-of-plane* atomic distances is expected because this kind of strain is performed maintaining the symmetry of the unit cell and, therefore, the cell tends to keep its volume. Although the MnGaN-2D atomic positions are significantly modified under different strains, the Mn states remain highly spin polarized and spin split, in all cases. This fact indicates the high stability of the MnGaN-2D monolayer magnetism even in the presence of lattice structural changes.

As can be seen in Fig. 6(a), the MnGaN-2D spin-polarized DOS is indeed significantly modified by *in-plane* isotropic strain. In fact, the FSMP originally at ~ -1.6 eV in the unstrained case, is shifted either to the left when compressing, or to the right when expanding. In the expanding case (18.9% areal strain), E_{FSMP} is shifted ~ 0.3 eV while the position of the empty states peak does not move noticeably. This shift of the Mn states resembles what was previously observed in the spectroscopy data of Fig. 4.

Spin-orbit calculations are also performed by considering the *in-plane* versus *out-of-plane* Mn spin orientations in order to explore the MnGaN-2D magnetic anisotropy and its relation to lattice strain. The energy differences are schematically presented in Fig. 6(b), at the right of each corresponding graph of Fig. 6(a), for the laterally expanded (tensile strain) case, unstrained, and laterally compressed lattices. For the unstrained (and laterally compressed) cases, we find that the energy is lower by 0.2 meV/Mn (and 0.06 meV/Mn) for the

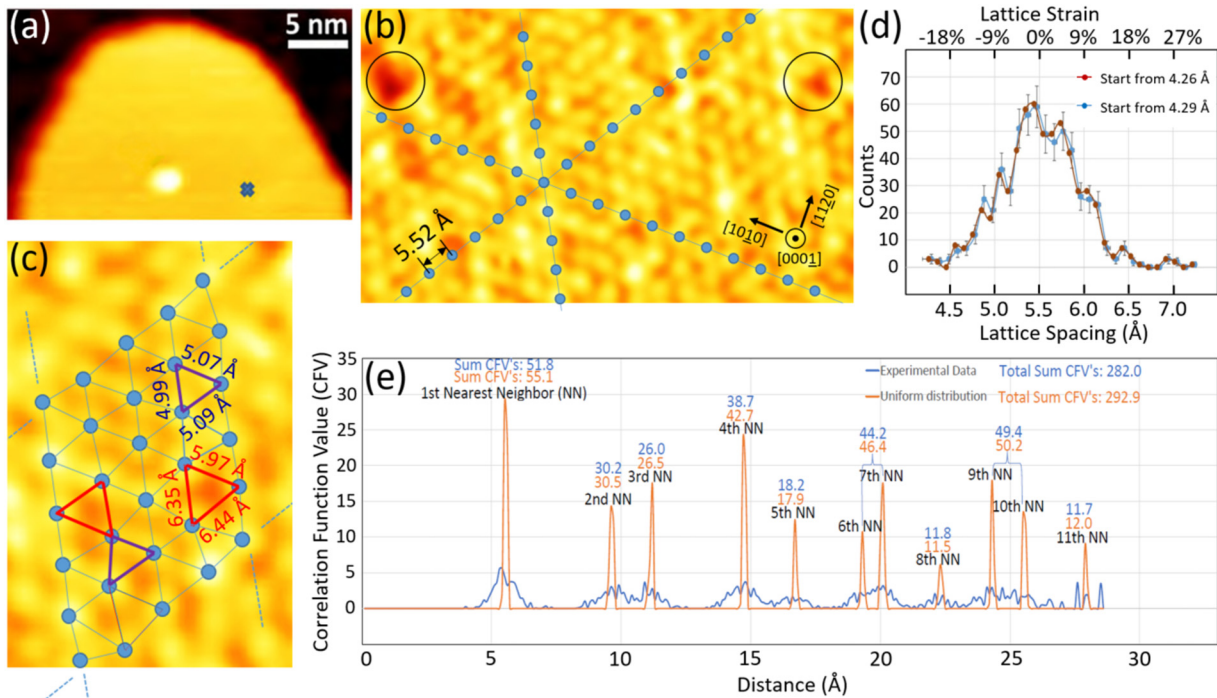


FIG. 5. (a) STM image ($V_s = -2.0$ V, $I = 100$ pA) of the MnGaN-2D area before the STS measurements shown in Fig. 4(a). The tip is fixed at the marked position while taking the dI/dV spectra. (b) Zoom-in STM image ($V_s = -1.3$ V, $I = 100$ pA) showing the hexagonal-like but irregular lattice structure of MnGaN-2D. Equally spaced dots along $(10\bar{1}0)$ azimuths show the long-range ordering; defects are encircled. (c) Tighter zoom-in STM image ($V_s = -1.3$ V, $I = 100$ pA) with dot-mesh overlay on atomic protrusions revealing the local disorder of the lattice. (d) Plot of the lattice spacing distribution for MnGaN-2D revealing its characteristic non-Gaussian shape with wide-ranging lattice spacings. (e) Two-point correlation function for the MnGaN-2D lattice plotted together with that of a uniform hexagonal lattice.

out-of-plane spin configuration, in agreement with the SQUID results presented in Fig. 2. But for the laterally expanded (tensile) case, the *in-plane* Mn spin configuration is energetically favored over the *out-of-plane* case by 0.15 meV/Mn. Therefore, although the energy differences are small, our lateral isotropic calculations suggest magnetoelasticity for the MnGaN-2D structure.

2. Local anisotropic model: Axial strain

Taking into account the local disorder observed in the STM images of Figs. 1 and 5, evidenced in the lattice-spacing distribution, in this section we explore whether local strain could influence the peak locations of the Mn PDOS. For this purpose, we modify the atomic positions surrounding a Mn atom. As the Ga adatoms' first Mn atom neighbors are along the $[10\bar{1}0]$ direction, we create axial strain by varying the spacing between Ga adatoms along that direction (we name this spacing as d). In this way, we generate either compressive or tensile local strain in the vicinity of a Mn atom.

We take a MnGaN-2D 2×2 supercell with lateral lattice parameter of $2a$ where $a = \sqrt{3} \times a_{\text{GaN}}$ which then has four Mn atoms, labeled as Mn_1 , Mn_2 , Mn_3 , and Mn_4 [see Fig. 7(a)]. To produce strictly local distortions around one particular Mn atom (namely, Mn_1), we vary the spacing between Ga adatoms surrounding Mn_1 and call it $d = d_1$. This procedure, in turn, changes the distance between Ga adatoms around Mn_2 (referenced as d_2) because the sum of d_1 and d_2 is fixed by the length of the supercell, that is, $d_1 + d_2 = 2a$ [see Fig. 7(a)].

Note that varying d_1 (and consequently d_2) directly changes the strain around both Mn_1 and Mn_2 . Once d_1 and d_2 are fixed, all the other atoms in the cell are relaxed. In this way, the local strain environments of all four Mn atoms in

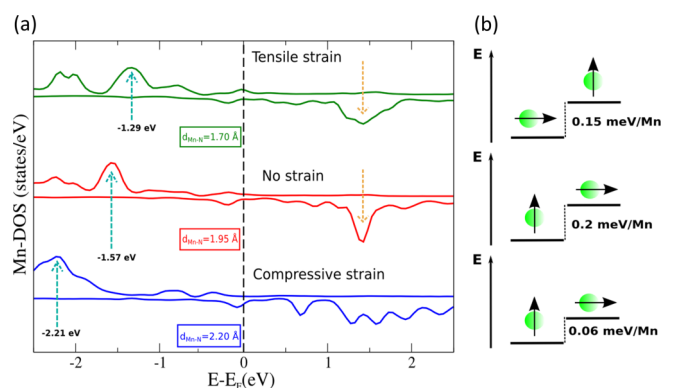


FIG. 6. Lateral isotropic strain effect on the MnGaN-2D electronic structure. (a) The calculated spin-polarized, Mn PDOS for lateral expansion, no strain, and lateral compression are shown in the top, middle, and bottom panels, respectively. (b) Magnetic anisotropic energy (MAE) obtained with first-principles spin-orbit calculations. The energy differences for each case on the left in (a) are shown on the right in (b). Schematically depicted are the *in-plane* (\rightarrow) and *out-of-plane* (\uparrow) axes considered in the calculations. The energy differences shown correspond to the lowest-energy solutions for each case.

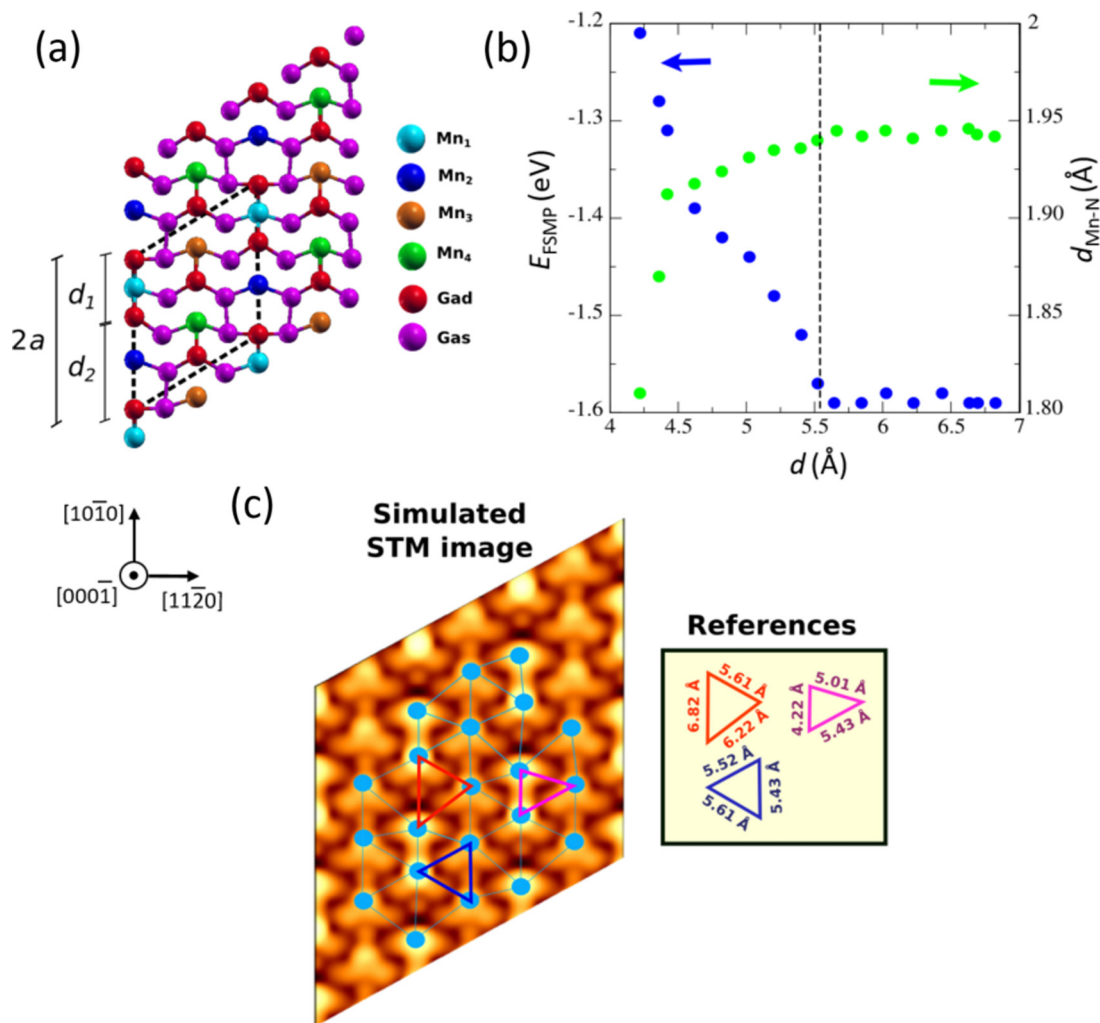


FIG. 7. (a) Top view of the MnGaN-2D 2×2 supercell used in the calculations. The distances d_1 and d_2 are shown (see text). (b) Plots of the filled-states Mn PDOS peak energy (E_{FSMP}) and Mn-N bond length ($d_{\text{Mn-N}}$) as functions of the distance d between neighboring Ga atoms along the $[10\bar{1}0]$ direction. This distance d equals d_1 for the case of Mn₁ and d_2 for the case of Mn₂. In particular, d is d_1 for the range $[4.22\text{--}5.52 \text{ \AA}]$, while it is d_2 for the range $[5.52\text{--}6.82 \text{ \AA}]$. The unstrained d value is marked by the vertical dashed line. (c) Tersoff-Hamann image for simulated anisotropic strain effect for the particular case of $d_1 = 4.23 \text{ \AA}$ and $d_2 = 6.82 \text{ \AA}$. The different Ga distances d are shown at the sides of the triangles; those d values along the y -axis direction $[10\bar{1}0]$ are associated with strain at the Mn atoms.

the 2×2 cell are allowed to change, but the effect is indeed local as the environments of Mn₃ and Mn₄ remain almost the same after relaxation. It is important to note that this procedure breaks the symmetry of the underlying hexagonal cell as we want to investigate local disorder. Specifically, to study the effect of this kind of disorder on E_{FSMP} , we plot in Fig. 7(b) E_{FSMP} as a function of the Ga adatom spacing d . As for each calculation we get different environments around Mn₁ and Mn₂ atoms, we generically take the d variable that will be $d = d_1$ for the lower range ($4.22\text{--}5.52 \text{ \AA}$), and $d = d_2$ for the upper range ($5.52\text{--}6.82 \text{ \AA}$). We take $d = 5.52 \text{ \AA}$ as the unstrained reference and mark it with a dashed line in Fig. 7(b).

It is seen that both E_{FSMP} and the Mn-N distance ($d_{\text{Mn-N}}$) depend strongly on the local d spacing over the lower range (locally compressing along $[10\bar{1}0]$), whereas they are not strong functions of d over the upper range (locally expanding along $[10\bar{1}0]$). As d decreases from 5.52 \AA down to 4.22 \AA , E_{FSMP} rapidly increases while $d_{\text{Mn-N}}$ decreases, slowly at first,

then rapidly below $d \sim 4.4 \text{ \AA}$. Therefore, if we consider E_{FSMP} as a function of $d_{\text{Mn-N}}$, both isotropic and anisotropic models give the same, consistent behavior in which E_{FSMP} increases with decreasing $d_{\text{Mn-N}}$.

Figure 7(b) shows that local compressive strain leads to positive (rightward) shifts of E_{FSMP} starting from -1.59 eV and going up to -1.21 eV . This behavior is in relative good quantitative agreement with the STS observations seen in Fig. 4 where the FSMP shifts to the right over a range from -1.69 eV up to -1.22 eV . We also notice that the lower d -spacing (compressive) range over which this strong peak energy variation occurs ($4.22\text{--}5.65 \text{ \AA}$) matches approximately the local compressive strain range from the STM measurements ($4.25\text{--}5.50 \text{ \AA}$) as seen in Fig. 5(d). Furthermore, we see from Fig. 7(b) that E_{FSMP} becomes flat at $\sim -1.59 \text{ eV}$ (i.e., no leftward shift of the peak) for expanding local *in-plane* strain, consistent with the fact that leftward shifts are not seen in the STM dI/dV data. This is different compared to the isotropic model which also predicts leftward shifts of E_{FSMP} . This result

further confirms that the E_{FSMP} shift is really a function of the *out-of-plane* strain in the Mn-N bond.

Figure 7(c) shows the Tersoff-Hamann (TH) [37] simulated STM image for a typical anisotropic strained surface. It should be noted that this simulation is only for a single uniaxial domain of MnGaN-2D structure within a 2×2 supercell, whereas the real surface would contain presumably a random intermixing of domains due to the underlying GaN's threefold symmetry. But if we compare the anisotropic TH simulation with the atomic resolution STM data from Fig. 5(c), we get qualitative agreement in which two Ga adatoms closer together (compressive strain) appear as more of an elongated, merged, and brighter shape with such features appearing both in the experimental images and the simulated ones. It is at these compressive strained locations where we would expect to see the positive shifts of E_{FSMP} .

IV. CONCLUSIONS

To conclude, we have found that the MnGaN-2D magnetic monolayer on GaN(000 $\bar{1}$) has an intrinsic strain-dependent PDOS, in which the most important effect is that the compression of the Mn-N bond length leads to an energy shift of the occupied-states spin-polarized Mn peak. This shift, predicted theoretically, is also observed in our experimental tunneling spectroscopy data. Our atomic resolution STM images also confirm a distribution of both compressive and expansive strains.

Our isotropic calculations predict that the rightward shift of the filled-states Mn PDOS peak switches the MnGaN-2D

magnetic anisotropy from having normally PMA to having *in-plane* magnetic anisotropy due to expanded lateral strain. However, in the anisotropic model, the rightward shift of the Mn peak corresponds instead to *in-plane* compressive strain as well as *out-of-plane* compressive strain.

The distribution of strain states within the surface is consistent with our results from SQUID magnetometry which reveal PMA with an *out-of-plane* magnetic anisotropy angle of $\sim 54^\circ$. The clear ferromagnetic hysteresis observed for MnGaN-2D by SQUID at both 10 and 300 K is verified by comparison to control samples of just GaN layers on sapphire. These results regarding the strain-dependent magnetic density of states and possible magnetoelasticity of MnGaN-2D open future possibilities for magnetic strain engineering of this 2D system which could have important technological applications such as for advanced spintronic devices operating at room-temperature.

ACKNOWLEDGMENTS

Research supported by the US Department of Energy, Office of Basic Energy Sciences, Division of Materials Sciences and Engineering under Award No. DE-FG02-06ER46317 (scanning tunneling microscopy studies) and Award No. DE-SC0001304 (magnetization measurements). D.H., M.A.B., and V.F. acknowledge CONICET for financial support (density functional theory calculations). Authors additionally acknowledge RHK Technology for use of the R9 STM electronics as well as the RHK data acquisition and image processing software.

-
- [1] D. Sando, A. Agbelele, D. Rahmedov, J. Liu, P. Rovillain, C. Toulouse, I. C. Infante, A. P. Pyatakov, S. Fusil, E. Jacquet *et al.*, Crafting the magnonic and spintronic response of BiFeO₃ films by epitaxial strain, *Nat. Mater.* **12**, 641 (2013).
 - [2] R. Fei and L. Yang, Strain-engineering the anisotropic electrical conductance of few-layer black phosphorus, *Nano Lett.* **14**, 2884 (2014).
 - [3] A. Castellanos-Gomez, R. Roldán, E. Cappelluti, M. Buscema, F. Guinea, H. S. J. van der Zant, and G. A. Steele, Local strain engineering in atomically thin MoS₂, *Nano Lett.* **13**, 5361 (2013).
 - [4] C. Lee, X. Wei, J. W. Kysar, and J. Hone, Measurement of the elastic properties and intrinsic strength of monolayer graphene, *Science* **321**, 385 (2008).
 - [5] S. Bertolazzi, J. Brivio, and A. Kis, Stretching and breaking of ultrathin MoS₂, *ACS Nano* **5**, 9703 (2011).
 - [6] N. Levy, S. A. Burke, K. L. Meaker, M. Panlasigui, A. Zettl, F. Guinea, A. H. Castro Neto, and M. F. Crommie, Strain-induced pseudo magnetic fields greater than 300 tesla in graphene nanobubbles, *Science* **329**, 544 (2010).
 - [7] F. Guinea, M. I. Katsnelson, and A. K. Geim, Energy gaps and a zero-field quantum Hall effect in graphene by strain engineering, *Nat. Phys.* **6**, 30 (2010).
 - [8] M. N. Baibich, J. M. Broto, A. Fert, F. Nguyen Van Dau, F. Petroff, P. Etienne, G. Creuzet, A. Friederich, and J. Chazelas, Giant Magnetoresistance of (001) Fe/(001) Cr Magnetic Superlattices, *Phys. Rev. Lett.* **61**, 2472 (1988).
 - [9] G. Binasch, P. Grünberg, F. Saurenbach, and W. Zinn, Enhanced magnetoresistance in layered magnetic structures with antiferromagnetic interlayer exchange, *Phys. Rev. B* **39**, 4828 (1989).
 - [10] T. Miyazaki and N. Tezuka, Giant magnetic tunneling effect in Fe/Al₂O₃/Fe junction, *J. Magn. Magn. Mater.* **139**, L231 (1995).
 - [11] J. S. Moodera, L. R. Kinder, T. M. Wong, and R. Meservey, Large Magnetoresistance at Room Temperature in Ferromagnetic Thin Film Tunnel Junctions, *Phys. Rev. Lett.* **74**, 3273 (1995).
 - [12] L. Berger, Emission of spin waves by a magnetic multilayer traversed by a current, *Phys. Rev. E* **54**, 4828 (1996).
 - [13] J. C. Slonczewski, Current-driven excitation of magnetic multilayers, *J. Magn. Magn. Mater.* **159**, L1 (1996).
 - [14] S. A. Wolf, D. D. Awschalom, R. A. Buhrman, D. M. Daughton, S. von Molnar, M. L. Roukes, A. Y. Chtchelkanova, and D. M. Treger, Spintronics: A spin-based electronics vision for the future, *Science* **294**, 1488 (2001).
 - [15] I. Zutic, J. Fabian, and S. Das Sarma, Spintronics: Fundamentals and applications, *Rev. Mod. Phys.* **76**, 323 (2004).
 - [16] Y. C. Cheng, Z. Y. Zhu, W. B. Mi, Z. B. Guo, and U. Schwingenschlögl, Prediction of two-dimensional diluted magnetic semiconductors: Doped monolayer MoS₂ systems, *Phys. Rev. B* **87**, 100401(R) (2013).

- [17] C. Gong, L. Li, Z. Li, H. Ji, A. Stern, Y. Xia, T. Cao, W. Bao, C. Wang, Y. Wang, Z. Q. Qiu, R. J. Cava, S. G. Louie, J. Xia, and X. Zhang, Discovery of intrinsic ferromagnetism in two-dimensional van der Waals crystals, *Nature (London)* **546**, 265 (2017).
- [18] B. Huang, G. Clark, E. Navarro-Moratalla, D. R. Klein, R. Cheng, K. L. Seyler, D. Zhong, E. Schmidg, M. A. McGuire, D. H. Cobden, W. Yao, D. Xiao, P. Jarillo-Herrero, and X. Xu, Layer-dependent ferromagnetism in a van der Waals crystal down to the monolayer limit, *Nature (London)* **546**, 270 (2017).
- [19] Y. Ma, A. V. Chinchore, A. R. Smith, M. A. Barral, and V. Ferrari, A two-dimensional manganese gallium nitride surface structure showing ferromagnetism at room temperature, *Nano Lett.* **18**, 158 (2018).
- [20] D. J. OHara, T. Zhu, A. H. Trout, A. S. Ahmed, Y. K. Luo, C. H. Lee, M. R. Brenner, S. Rajan, J. A. Gupta, D. W. McComb, and R. K. Kawakami, Room temperature intrinsic ferromagnetism in epitaxial manganese selenide films in the monolayer limit, *Nano Lett.* **18**, 3125 (2018).
- [21] M. Bonilla, S. Kolekar, Y. Ma, H. C. Diaz, V. Kalappattil, R. Das, T. Eggers, H. R. Gutierrez, M.-H. Phan, and M. Batzill, Strong room-temperature ferromagnetism in VSe₂ monolayers on van der Waals substrates, *Nat. Nanotechnol.* **13**, 289 (2018).
- [22] A. V. Chinchore, K. Wang, M. Shi, A. O. Mandru, Y. Liu, M. Haider, A. R. Smith, V. Ferrari, M. A. Barral, and P. Ordejón, Manganese 3×3 and $\sqrt{3} \times \sqrt{3} - R30^\circ$ structures and structural phase transition on *w*-GaN(000 $\bar{1}$) studied by scanning tunneling microscopy and first-principles theory, *Phys. Rev. B* **87**, 165426 (2013).
- [23] J. A. Stroscio, R. M. Feenstra, and A. P. Fein, Electronic Structure of the Si (111) 2×1 Surface by Scanning-Tunneling Microscopy, *Phys. Rev. Lett.* **57**, 2579 (1986).
- [24] R. M. Feenstra, Tunneling spectroscopy of the (110) surface of direct-gap III-V semiconductors, *Phys. Rev. B* **50**, 4561 (1994).
- [25] D. M. Ceperley and B. J. Adler, Ground State of the Electron Gas by a Stochastic Method, *Phys. Rev. Lett.* **45**, 566 (1980).
- [26] J. P. Perdew and A. Zunger, Self-interaction correction to density-functional approximations for many-electron systems, *Phys. Rev. B* **23**, 5048 (1981).
- [27] N. Troullier and J. L. Martins, Efficient pseudopotentials for plane-wave calculations, *Phys. Rev. B* **43**, 1993 (1991).
- [28] L. Kleinman and D. M. Bylander, Efficacious Form for Model Pseudopotentials, *Phys. Rev. Lett.* **48**, 1425 (1982).
- [29] S. G. Louie, S. Froyen, and M. L. Cohen, Nonlinear ionic pseudopotentials in spin-density-functional calculations, *Phys. Rev. B* **26**, 1738 (1982).
- [30] J. M. Soler, E. Artacho, J. D. Gale, A. Garcia, J. Junquera, P. Ordejón, and D. Sánchez-Portal, The SIESTA method for *ab initio* order-N materials simulation, *J. Phys.: Condens. Matter* **14**, 2745 (2002).
- [31] H. A. H. Al-Britthen, R. Yang, M. B. Haider, C. Constantin, E. Lu, N. Sandler, A. R. Smith, and P. Ordejón, Scanning Tunneling Microscopy and Surface Simulation of Zinc-Blende GaN(001) Intrinsic $4 \times$ Reconstruction: Linear Gallium Tetramers?, *Phys. Rev. Lett.* **95**, 146102 (2005).
- [32] V. Ferrari, J. M. Pruneda, and E. Artacho, Density functionals and half metallicity in La_{2/3}Sr_{1/3}MnO₃, *Phys. Status Solidi A* **203**, 1437 (2006).
- [33] A. Dal Corso and A. Mosca Conte, Spin-orbit coupling with ultrasoft pseudopotentials: Application to Au and Pt, *Phys. Rev. B* **71**, 115106 (2005).
- [34] P. Giannozzi, S. Baroni, N. Bonini, M. Calandra, R. Car, C. Cavazzoni, D. Ceresoli, G. L. Chiarotti, M. Cococcioni, I. Dabo *et al.*, QUANTUM ESPRESSO: A modular and open-source software project for quantum simulations of materials, *J. Phys.: Condens. Matter* **21**, 395502 (2009).
- [35] See Supplemental Material at <http://link.aps.org/supplemental/10.1103/PhysRevMaterials.4.064006> for *I/V* and *dI/dV* curve data corresponding to Fig. 4.
- [36] I. Valmianski, Matlab application: Two point correlation function of a finite 2D lattice (MATLAB Central/Mathworks, Natick, MA, 2011).
- [37] J. Tersoff and D. R. Hamann, Theory and Application for the Scanning Tunneling Microscope, *Phys. Rev. Lett.* **50**, 1998 (1983).